Phonon-mediated superconductivity in ternary silicides X_4CoSi (X = Nb, Ta)

Jonas Bekaert*

Department of Physics and NANOlab Center of Excellence, University of Antwerp, Groenenborgerlaan 171, B-2020 Antwerp, Belgium

(Received 1 June 2023; revised 25 September 2023; accepted 28 September 2023; published 17 October 2023)

The superconducting properties of two recently synthesized ternary silicides with unit formula X_4CoSi (X = Nb, Ta) are investigated through *ab initio* calculations combined with Eliashberg theory. Interestingly, their crystal structure comprises interlocking honeycomb networks of Nb/Ta atoms. Nb_4CoSi is found to harbor better conditions for phonon-mediated superconductivity, as it possesses a higher density of states at the Fermi level, fostering stronger electron-phonon coupling. The superconducting critical temperatures (T_c) follow the same trend, with Nb_4CoSi having a twice higher value than Ta_4CoSi. Furthermore, the calculated T_c values (5.9 K vs 3.1 K) agree excellently with the experimentally obtained ones, establishing superconductivity in this new materials class as mediated by the electron-phonon coupling. Furthermore, my calculations show that the superconducting properties of these compounds do not simply correlate with the parameters of their honeycomb networks, contrary to proposals raised in the literature. Rather, their complete fermiology and phonon spectrum should be taken into account in order to explain their respective superconducting properties.

DOI: 10.1103/PhysRevB.108.134504

I. INTRODUCTION

Ternary silicide intermetallic compounds are comprised of silicon together with two different metallic elements. They were found to harbor highly diverse physical properties, including heavy-fermion superconductivity in $CeRhSi_3$ [1], two-gap superconductivity in $X_2Fe_3Si_5$ (X = Sc, Lu) and $Sc_5Ir_4Si_{10}$ [2,3], and large magnetoresistance in $NdCo_2Si_2$ [4].

Recently, a new member of this materials family, Ta_4CoSi, was synthesized for the first time [5]. Based on resistivity and magnetic susceptibility measurements, it was found to be a superconductor with a critical temperature (T_c) of 2.45 K. Nb_4MSi (M = Ni, Co, Fe) compounds with the same crystal structure, characterized by the centrosymmetric tetragonal space group $P4/mcc$ (No. 124), were also found to display superconductivity [6]. In the case of Nb_4CoSi, T_c reaches 6.0 K, while the T_c's of Nb_4FeSi (6.8 K) and Nb_4NiSi (7.7 K) are slightly higher.

Interestingly, these X_4MSi bulk materials host honeycomb networks composed of niobium or tantalum atoms [5,6], though they are not occurring as distinct layers unlike the honeycomb boron networks in the two-gap superconductor MgB_2 [7]. Other superconductors hosting honeycomb networks are mainly situated in low-dimensional systems, such as lithium- and calcium-doped graphene [8–10], and gallenene [11].

In their recent work on Ta_4CoSi, Zeng *et al.* propose a linearly decreasing relation between T_c and the interatomic distance within the honeycomb network, based on available values for a few superconducting compounds with a honeycomb network, ternary silicides, and others [5]. However, this apparent relation is rather counterintuitive, as biaxial tensile strain—whereby the interatomic distances increase—tends to have the opposite effect. Namely, the resulting attenuation of the interatomic electron clouds leads to phonon softening, which can enhance the electron-phonon coupling and T_c, according to Eliashberg theory. Systems for which this effect has been demonstrated include materials with a honeycomb network, such as doped graphene [12], and monolayer MgB_2 in pristine and hydrogenated form [13,14].

Here, using first-principles calculations of electronic structure, phonons, and their interaction, I demonstrate that superconductivity in this class of ternary silicides is conventional in nature. To this end, I show that the T_c is correctly predicted by Eliashberg theory, indicating the absence of unconventional effects, like heavy-fermion superconductivity. I also set out to explain the difference in T_c between Ta_4CoSi and Nb_4CoSi, and to elucidate the role of their respective honeycomb networks, and of the spin-orbit coupling, being stronger for tantalum than for niobium.

II. METHODS

The calculations were performed within density functional theory, as implemented within the ABINIT code [15], using the Perdew-Burke-Ernzerhof functional [16]. Fully relativistic optimized norm-conserving pseudopotentials from the PseudoDojo project were used to include spin-orbit coupling (SOC). The valence electron configurations of the used pseudopotentials are Nb-$4s^24p^64d^45s^1$, Ta-$5s^25p^65d^36s^2$, Co-$3s^23p^63d^74s^2$, and Si-$3s^23p^2$. For all the calculations, an energy cutoff value of 50 Ha for the plane-wave basis, and a $12 \times 12 \times 16$ k grid were used. Gaussian smearing was used for the electronic occupations around the Fermi level (E_F), with a smearing width of 0.01 Ha. The crystal structures were relaxed so all force components were below 5×10^{-6} Ha/bohr for each atom.

To calculate the phonon dispersions and the electron-phonon coupling (EPC), I used density functional perturbation

*jonas.bekaert@uantwerpen.be

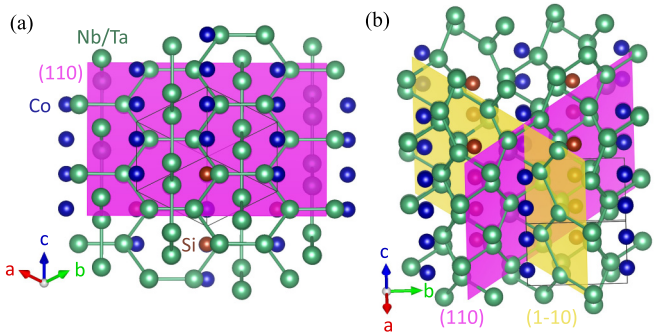

FIG. 1. Crystal structure of Nb_4CoSi and Ta_4CoSi. (a) Honeycomb network of Nb/Ta atoms within the (110) planes. (b) The two perpendicular, interlocking honeycomb networks within the (110) and $(1\bar{1}0)$ planes.

theory (DFPT) as implemented in ABINIT, using a $12 \times 12 \times 16$ electronic k grid and a $3 \times 3 \times 4$ phononic q grid. After thoroughly checking that its effect on the electronic structure near the Fermi level is very limited, SOC was omitted in the DFPT calculations, due to computational restrictions posed by the size of the unit cell. To characterize the superconducting state I employed the Migdal-Eliashberg theory for phonon-mediated superconductivity [17–19]. Using the density of states at the Fermi level (N_F), the matrix elements of the electron-phonon coupling ($g^{\nu}_{\mathbf{k},\mathbf{k}+\mathbf{q}}$), and the phononic ($\omega^{\nu}_{\mathbf{q}}$) and electronic ($\epsilon_{\mathbf{k}}$) dispersions—all of which were obtained from my *ab initio* calculations—I have evaluated the isotropic Eliashberg functions,

$$\alpha^2F(\omega) = \frac{1}{N_F}\sum_{\nu,\mathbf{k},\mathbf{q}} \left|g^{\nu}_{\mathbf{k},\mathbf{k}+\mathbf{q}}\right|^2 \delta\left(\omega - \omega^{\nu}_{\mathbf{q}}\right)\delta(\epsilon_{\mathbf{k}})\delta(\epsilon_{\mathbf{k}+\mathbf{q}}), \quad (1)$$

TABLE I. Comparison of calculated and experimental lattice parameters of Nb_4CoSi and Ta_4CoSi. Theoretical values from this work are indicated by "TW". Experimental values stem from Ref. [6] ("EXPI") for Nb_4CoSi, and from Ref. [5] ("EXPII") for Ta_4CoSi. d_1 and d_2 are the $X - X$ (X = Nb, Ta) distances within the honeycomb network.

Compound	Ref.	a (Å)	c (Å)	d_1 (Å)	d_2 (Å)
Nb_4CoSi	TW	6.21	5.02	2.81	2.97
Nb_4CoSi	EXPI	6.16	5.06	2.78	2.99
Ta_4CoSi	TW	6.21	4.99	2.82	2.95
Ta_4CoSi	EXPII	6.18	4.98	2.80	2.94

and the corresponding EPC constants by

$$\lambda = 2\int_0^{\infty} \alpha^2F(\omega)\omega^{-1}d\omega. \quad (2)$$

The summations in Eq. (1) were evaluated using Gaussian integration with a smearing value of 4×10^{-5} Ha. I subsequently calculated the superconducting T_c using the McMillan-Allen-Dynes formula [20–22]. Here, the screened Coulomb interaction between Cooper-pair electrons was treated through the Morel-Anderson pseudopotential μ^* [23], where a value of 0.13 was adopted, suitable for transition metal compounds with d electrons [24].

III. CRYSTAL STRUCTURE

The crystal structure of the ternary silicides is displayed in Fig. 1. The unit cell consists of two X_4CoSi formula units, hence it contains 12 atoms. As mentioned in the Introduction, these structures harbor networks of Nb/Ta atoms arranged in

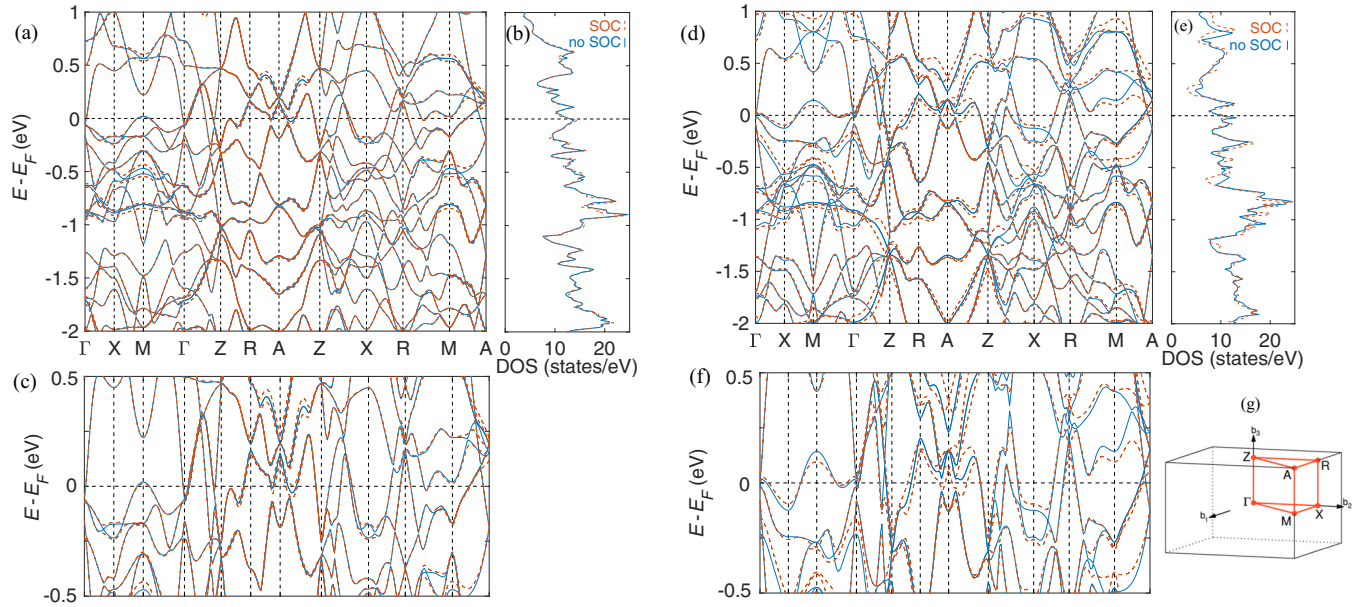

FIG. 2. (a) Electronic band structure of Nb_4CoSi and (b) the corresponding DOS. (c) Detail of the electronic band structure of Nb_4CoSi around E_F. (d) Electronic band structure of Ta_4CoSi and (e) the corresponding DOS. (f) Detail of the electronic band structure of Ta_4CoSi around E_F. The results are presented with and without inclusion of SOC, depicted by dashed orange lines and solid blue lines, respectively. (g) The tetragonal Brillouin zone with the high-symmetry points and the irreducible Brillouin zone (red) indicated [25].

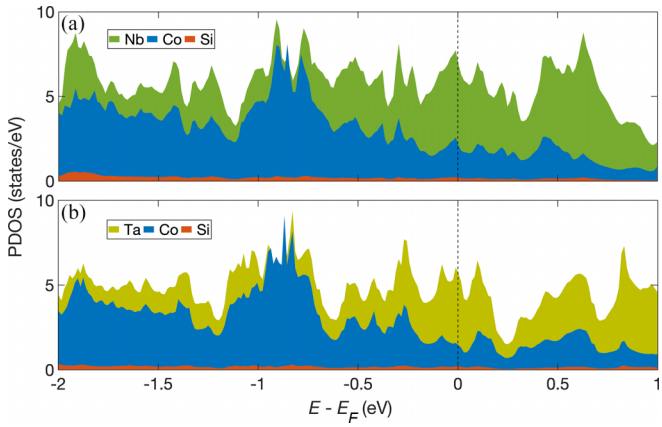

FIG. 3. Atom-resolved partial densities of states (PDOS) of (a) Nb_4CoSi and (b) Ta_4CoSi, obtained with inclusion of SOC.

a honeycomb lattice. The first honeycomb network is located within the (110) plane, as depicted in Fig. 1(a). As shown in Fig. 1(b), there is a second Nb/Ta honeycomb network in the $(1\bar{1}0)$ plane. As such, it is perpendicular to the first one, as well as interlocking with it, as can be clearly seen in Fig. 1(b).

The calculated lattice parameters of the two investigated compounds are summarized in Table I, and compared to the experimental values available in the literature [5,6]. An overall excellent agreement between theoretical and experimental values is obtained. Furthermore, I found that the inclusion of SOC does not affect the lattice parameters (a, c, d_1, and d_2) within a margin of 0.01 Å, for neither Nb_4CoSi nor Ta_4CoSi.

Since the Nb/Ta honeycomb networks are irregular, the hexagons possess two inequivalent sides, with lengths d_1 and d_2, as shown in Table I. Note that between Nb_4CoSi and Ta_4CoSi, d_1 increases slightly, while d_2 decreases—a trend agreed upon by the calculations and experiments. As a result, there is a small change in the anisotropy parameter d_1/d_2, from 94.6% in Nb_4CoSi to 95.6% in Ta_4CoSi. So, rather than a uniform change in lattice parameters of the honeycomb network—proposed in Ref. [5] to drive differences in T_c—there is a reduction of the anisotropy, going from Nb_4CoSi to Ta_4CoSi.

IV. ELECTRONIC STRUCTURE

As the second step towards the superconducting properties of Nb_4CoSi or Ta_4CoSi, we now take a look at their electronic structure. The band structures of both compounds are shown in Fig. 2, calculated with and without inclusion of SOC. In the case of Nb_4CoSi [see Fig. 2(a)], the changes in the band structure due to SOC are very limited. As a result, the DOS profiles with and without SOC, shown in Fig. 2(b), are nearly identical.

In the case of Ta_4CoSi, depicted in Fig. 2(d), more changes in the electronic structure occur upon inclusion of SOC, due to the higher atomic mass of Ta (with atomic number $Z = 73$). However, these are mainly situated away from E_F, in both the valence and the conduction region. Near E_F [cf. detail shown in Fig. 2(f)], the effect of SOC is limited to some changes in the band effective masses, and a few minor band splittings (e.g., along the path Z-R). As a result, the density of states (DOS) at E_F is almost identical with and without SOC [see Fig. 2(e)]. This enables us to evaluate the phonons, electron-phonon coupling, and the resulting superconducting properties without including SOC. Finally, I found that the DOS at E_F is significantly higher in the case of Nb_4CoSi than for Ta_4CoSi, namely, 13.10 states/eV compared to 10.22 states/eV.

To determine the individual atomic contributions to the electronic states near E_F, I have calculated the atom-resolved densities of states (with inclusion of SOC). Atomic spheres were defined as half of the nearest neighbor distances for each atomic type. The results depicted in Fig. 3 show that the Nb/Ta d states are the dominant contribution in the vicinity of the Fermi level. The second most important contribution is

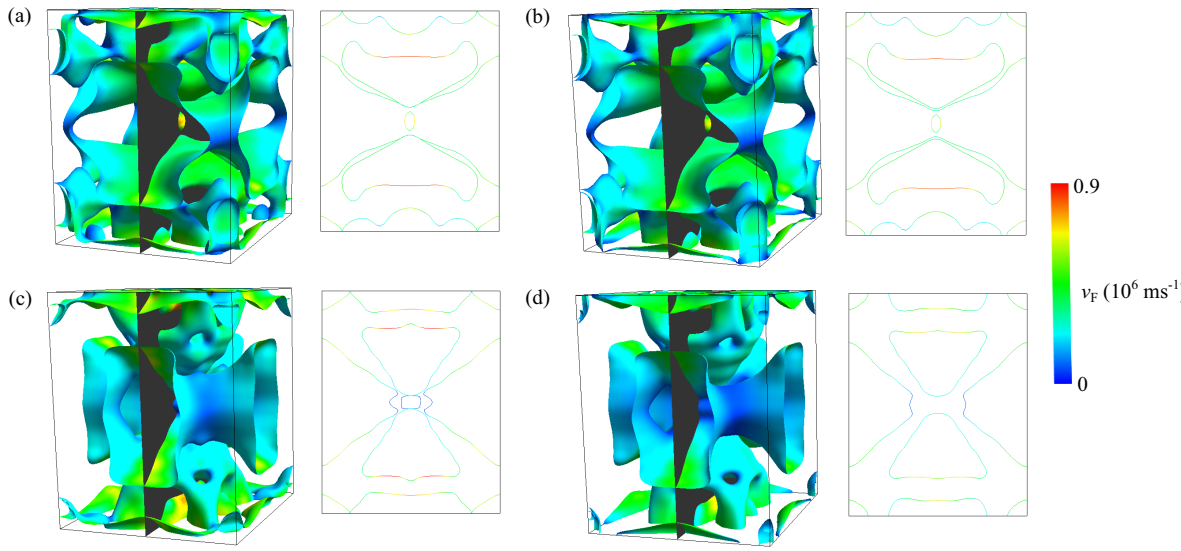

FIG. 4. Fermi surface and its (100) section (indicated by the gray plane), depicted within the Γ-centered Brillouin zone, for (a) Nb_4CoSi calculated without inclusion of SOC, and (b) with inclusion of SOC. The same properties for (c) Ta_4CoSi calculated without inclusion of SOC, and (d) with inclusion of SOC. The colors indicate the Fermi velocities (v_F).

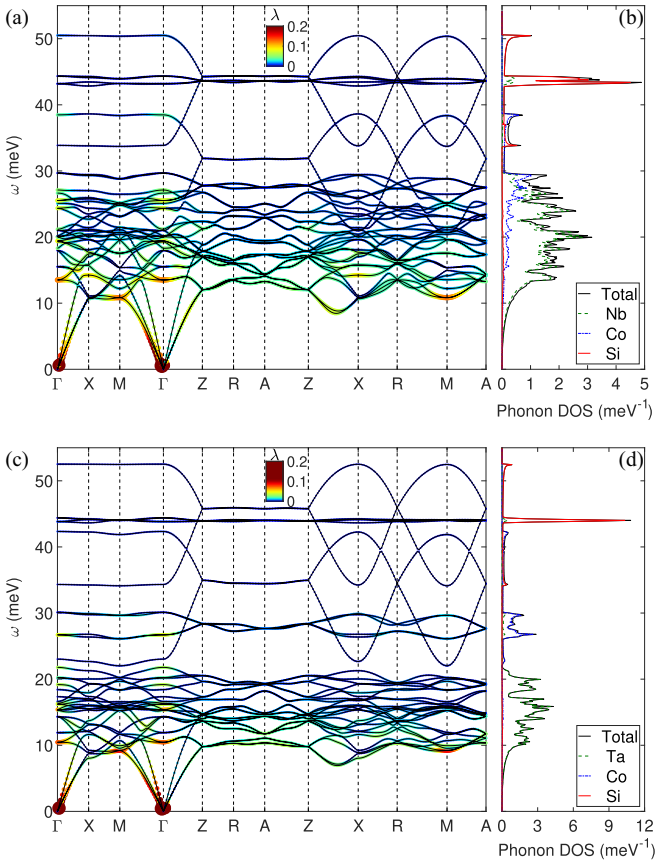

FIG. 5. Phonon band structure of (a) Nb_4CoSi and (c) Ta_4CoSi. The phonon-branch (ν) and **q**-point-resolved electron-phonon coupling $\lambda_{\mathbf{q}}^{\nu}$ is indicated by colors, as well as by point sizes (proportional to λ). (b) The corresponding phonon DOS—total as well as atom-resolved—of Nb_4CoSi and (d) Ta_4CoSi.

due to the Co d states. The fact that the majority of states at the Fermi level have d character justifies the choice of a μ^* value of 0.13 (cf. Sec. II).

The corresponding Fermi surfaces of both compounds are shown in Fig. 4, together with the Fermi velocities. Comparing the changes in the Fermi surface due to SOC, once again we clearly observe only minor variations in both the sheet composition and the Fermi velocities in the case of Nb_4CoSi [Fig. 4(a) vs 4(b)]. For Ta_4CoSi, more significant changes are found [Fig. 4(c) vs 4(d)], notably around the Brillouin zone vertex (point A), and center (Γ).

V. PHONONS AND ELECTRON-PHONON COUPLING

The vibrational properties of ternary silicides are interesting because of the presence of a very wide range of atomic masses, from very light elements such as Si ($Z = 14$), over intermediate mass elements such as Co ($Z = 27$), to heavy transition metals such as Nb ($Z = 41$) and Ta ($Z = 73$). The phonon dispersions of Nb_4CoSi and Ta_4CoSi are depicted in Figs. 5(a) and 5(c), respectively, and the corresponding atom-resolved phonon DOS in Figs. 5(b) and 5(d).

First of all, the phonon dispersions clearly demonstrate the dynamical stability of both compounds, without any phonon softening or Kohn anomalies that are known to occur in other transition metal compounds such as transition metal dichalcogenides. Due to the differences in atomic masses of Nb and Ta, the phonon DOSs show different hybridization behavior. Namely, Co hybridizes with both Nb and Si in Nb_4CoSi, whereas in Ta_4CoSi it only hybridizes with Si (to a very minor extent), leaving the Ta-based phonon modes entirely separated.

Furthermore, several of the Si- and Co-based phonon modes have a remarkably flat dispersion, leading to pronounced peaks in the phonon DOS at higher energies in both compounds. The presence of linear chains of Si and of Co atoms, located in between the interlocking honeycomb lattices, foster distinct longitudinal and transverse modes.

Figure 6(a) zooms in on the Si modes, and depicts several representative atomic displacements. In the Brillouin zone segment along Γ-X-M-Γ, two separate modes with a flat dispersion occur. Both modes have a longitudinal character, following the direction of the linear chain of Si atoms. The lower branch corresponds to in-phase movement of the two Si atoms within the unit cell, while the upper branch originates from out-of-phase movement. Another flat dispersion segment occurs along Z-R-A-Z, where the two modes become degenerate. Here, the phonon modes are as follows: (i) a single Si atom is moving while the other one stands still (along Z-R), and (ii) both atoms are moving in phase (at A). Along the segment Z-X-R-M, the displacements change from a single Si atom moving (at Z and R) to both Si atoms moving out of phase (at X and M), leading to significant dispersion. Finally, the other four modes consist of the transverse displacements of the Si atoms; an example is provided for the A point.

The mode- and momentum-resolved EPC is depicted on top of the phonon dispersion in Figs. 5(a) and 5(c). It reaches its highest values for the lower Nb- and Ta-based modes. On the other hand, the Si-based modes host almost no EPC. The analysis of the electronic structure in the previous section (Fig. 3) has also revealed that the electronic states near E_F have predominant transition metal d character, hence the EPC in these ternary silicides is mainly driven by Nb and Ta.

The phonon modes providing the main contributions to the EPC, predominantly due to Nb, are depicted in Fig. 6(b). The first optical mode at Γ ($\sim$14 meV) occurs in plane with respect to the honeycomb lattice, as does another strongly coupling mode at Γ (at $\sim$19 meV). On the other hand, other strongly coupling modes do not involve displacements within the honeycomb lattices, but rather out-of-plane deformations. For example, at Γ (at $\sim$24 meV), significant coupling is hosted by a radial breathing mode centered around the linear chains of Si atoms. Further strongly coupling modes occurring at other points of the Brillouin zone, such as at X ($\sim$14 meV) and M ($\sim$11 meV), likewise have an out-of-plane character with respect to the honeycomb lattices.

VI. SUPERCONDUCTIVITY

I now proceed to investigate the superconducting properties of Nb_4CoSi and Ta_4CoSi within the Eliashberg theory. Previous analysis of their superconducting T_c's was limited to models based on the Debye temperature (θ_D) [5], whereby $T_c \propto \theta_D$. It should be noted that this model is not very ade-

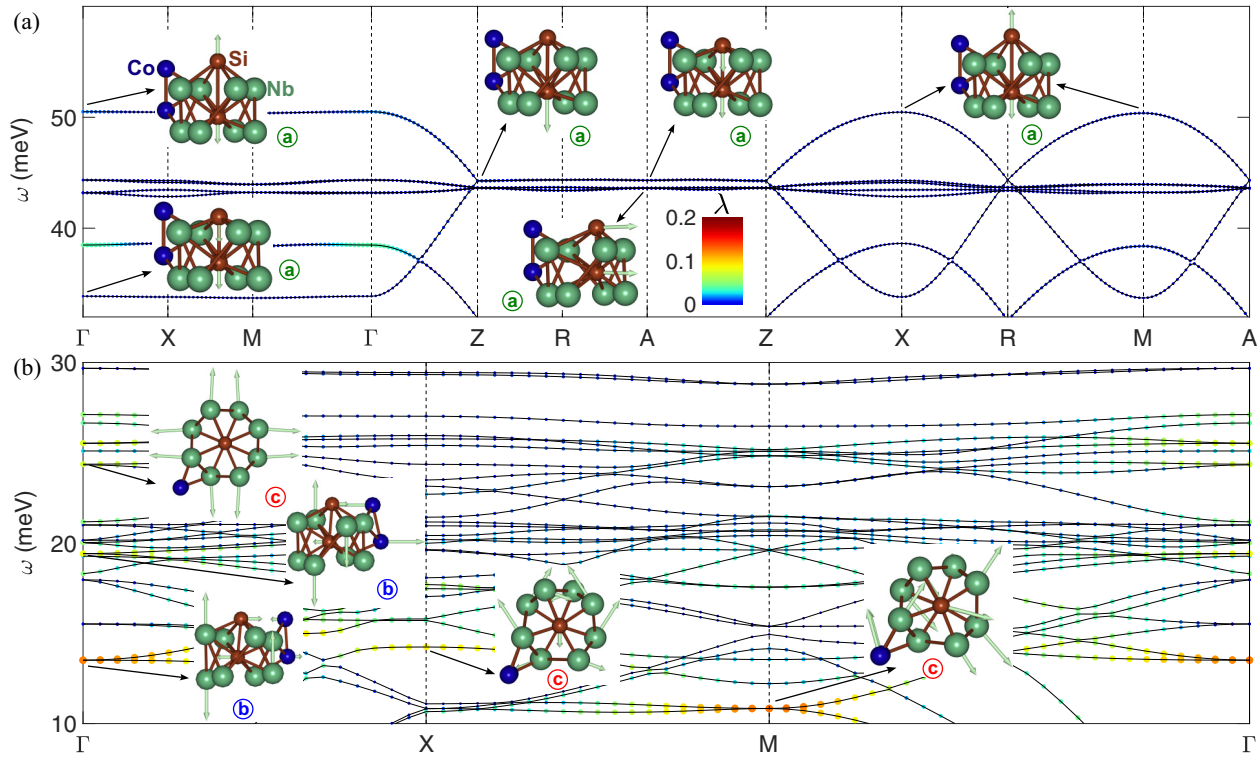

FIG. 6. (a) Detail of the higher-energy phonon dispersion of Nb_4CoSi, featuring mainly Si modes with a remarkable flat dispersion along certain Brillouin zone sections. The insets show the atomic displacements corresponding to specific eigenvalues $\omega_{\mathbf{q}}^{\nu}$ as indicated by the black arrows. (b) Similarly for lower-energy modes, dominated by Nb. Here, the modes with the most important contributions to the EPC were selected. The encircled **a**, **b**, and **c** indicate that the view is along this specified lattice vector.

quate for materials with an extended unit cell, as it is limited to acoustic modes. Instead, the logarithmically averaged phonon frequency $\omega_{\log}$, arising in Eliashberg theory, forms the core proportionality with T_c, as established in the Allen-Dynes adaptation of McMillan's formula [20–22].

As the first step, I calculated the Eliashberg spectral functions (α^2F) from my DFPT calculations according to Eq. (1). The results, depicted in Fig. 7, show that the main contributions to the Eliashberg functions occur below 30 meV in both ternary silicide compounds, and stem from the Nb/Ta- and Co-based phonon modes. In the case of Nb_4CoSi [Fig. 7(a)], their contributions are joined, with a dip at 22 meV, reflecting

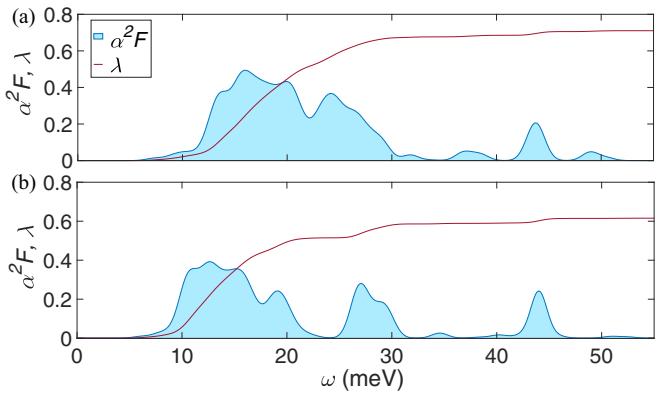

FIG. 7. Eliashberg function (α^2F) and electron-phonon coupling function (λ) of (a) Nb_4CoSi and (b) Ta_4CoSi.

the depletion in the phonon DOS at that energy [cf. Fig. 5(b)]. The case of Ta_4CoSi [Fig. 7(b)] presents a more pronounced separation of the contributions of Ta and Co, leading to two distinct domes in the Eliashberg function below 35 meV. This separation originates from the higher atomic mass of Ta, pushing its phonon modes to lower energies. This effects a reduction of the hybridization with the Co-based phonon modes (as explained in the preceding section).

The corresponding electron-phonon coupling functions (λ), obtained from the Eliashberg functions using Eq. (2), are also shown in Fig. 7. It is apparent that the total λ of Nb_4CoSi (0.71) significantly exceeds that of Ta_4CoSi (0.62). This stronger EPC in Nb_4CoSi clearly correlates with its higher N_F. Together with its higher $\omega_{\log}$, this results in a higher T_c, as obtained from the McMillan-Allen-Dynes formula. The obtained T_c of Nb_4CoSi is 5.9 K, compared to 3.1 K for Ta_4CoSi, in perfect agreement with their experimental values of 6.0 [5] and 2.45 K [5], respectively. These results are summarized in Table II.

Note that in this work the superconducting properties have been treated within an isotropic approximation for the superconducting gap. The excellent agreement between the experimental T_c values and those obtained here using isotropic Eliashberg theory strongly suggests the single-gap nature of superconductivity in these compounds. This is further corroborated by the composition of the Fermi surfaces, featuring a plethora of entangled Fermi sheets (see Fig. 4). Such highly connected Fermi surface renders the occurrence of distinct gaps on different Fermi sheets rather unlikely. This

TABLE II. Superconducting properties of Nb_4CoSi and Ta_4CoSi. Theoretical values from this work are indicated by "TW". Experimental values stem from Ref. [6] ("EXPI") for Nb_4CoSi, and from Ref. [5] ("EXPII") for Ta_4CoSi. The DOS at E_F (N_F) is given per 12-atom unit cell. The Morel-Anderson pseudopotential used to calculate T_c is $\mu^* = 0.13$.

Compound	Ref.	N_F (eV^{-1})	ω_{log} (K)	λ	T_c (K)
Nb_4CoSi	TW	13.10	213	0.71	5.9
Nb_4CoSi	EXPI				6.0
Ta_4CoSi	TW	10.22	177	0.62	3.1
Ta_4CoSi	EXPII				2.45

has, among others, been demonstrated through anisotropic Eliashberg calculations comparing mono- vs few-layer MgB_2 structures [13] and different phases of gallenene [11]. Nevertheless, there may be some degree of anisotropy of the superconducting gap across the Brillouin zone, whose main features may follow the distribution of the Fermi velocities shown in Fig. 4, as proposed by Saunderson *et al.* [26]. This could be further investigated through a fully anisotropic calculation within the density functional theory for superconductors (SCDFT) [27], UPPSC [14,28,29], or EPW [30] frameworks.

Finally, let us briefly discuss the potential effect of SOC on the superconducting properties. The electronic DOS of Ta_4CoSi with and without the inclusion of SOC is highly similar in the vicinity of the Fermi level, as can be seen in Fig. 2(e). The DOS at the Fermi level (N_F) obtained with the inclusion of SOC is merely 3.8% higher than the value obtained without SOC. Within the approximation that the inclusion of SOC exclusively results in this slight increase of N_F, one can estimate that λ is slightly enhanced from 0.62 to 0.64 and T_c from 3.1 to 3.5 K due to the inclusion of SOC.

VII. CONCLUSIONS

I performed an *ab initio* investigation of the structural, electronic, vibrational, and superconducting properties of two intermetallic ternary silicide compounds with unit formula X_4CoSi, differing only by the X element, being Nb or Ta. These recently synthesized compounds have been attracting significant interest in view of their transition metal honeycomb networks and experimentally observed superconductivity [5].

I found that both compounds harbor a rich fermiology in the vicinity of the Fermi level, characterized by a multitude of intersecting Fermi sheets (see Fig. 4). Between them, Nb_4CoSi has a 28% higher DOS at the Fermi level, leading to enhanced EPC compared to Ta_4CoSi (14% higher). Here, the higher mass of the Ta atoms mitigates the discrepancy in the EPC between the two compounds. Namely, it shifts the Eliashberg function to a lower phonon energy range (see Fig. 7), where it contributes more effectively to the EPC constant (λ). Nevertheless, due to the exponential dependence of T_c on λ, this leads to a marked difference in T_c values, 5.9 vs 3.1 K for Nb_4CoSi and Ta_4CoSi, respectively, agreeing very well with the experimentally obtained values (6.0 and 2.45 K [5,6]).

Due to the excellent agreement with the experimental T_c values, my calculations provide strong evidence for the conventional nature of superconductivity in these compounds. As explained above, I found that the main factor driving the difference in T_c between the Nb- and the Ta-based compound is their intrinsic difference in DOS at their respective Fermi levels. No direct link to the lattice parameters of their transition metal honeycomb networks was found, contrary to recent proposals raised in the literature [5]. The reasons for the absence of such link are that (i) the honeycomb network is irregular and does not change uniformly between different silicide compounds (rather, its anisotropy changes) and (ii) my Eliashberg calculations show that the electron-phonon coupling results from a multitude of electronic and phononic states, not just those directly related to the honeycomb networks, indicating the inadequacy of a simple Debye-type model [5]. Moreover, the role of SOC in the normal-state electronic as well as the superconducting properties is limited for both compounds (and especially so in the case of Nb_4CoSi).

These results emphasize the importance of taking into account the complete fermiology and phonon spectrum to calculate the superconducting properties of complex intermetallic compounds, as well as the significant role therein of the atomic masses of the constituent transition metal elements.

ACKNOWLEDGMENTS

J.B. acknowledges support as a Senior Postdoctoral Fellow of Research Foundation-Flanders (FWO, Fellowship No. 12ZZ323N). The computational resources and services were provided by the VSC (Flemish Supercomputer Center), funded by the FWO and the Flemish Government–department EWI.

[1] N. Kimura, K. Ito, K. Saitoh, Y. Umeda, H. Aoki, and T. Terashima, Pressure-induced superconductivity in noncentrosymmetric heavy-fermion $CeRhSi_3$, Phys. Rev. Lett. **95**, 247004 (2005).

[2] Y. Nakajima, T. Nakagawa, T. Tamegai, and H. Harima, Specific-heat evidence for two-gap superconductivity in the ternary-iron silicide $Lu_2Fe_3Si_5$, Phys. Rev. Lett. **100**, 157001 (2008).

[3] T. Tamegai, Y. Nakajima, T. Nakagawa, G. Li, and H. Harima, Two-gap superconductivity in $R_2Fe_3Si_5$ (R = Lu, Sc) and $Sc_5Ir_4Si_{10}$, Sci. Technol. Adv. Mater. **9**, 044206 (2008).

[4] R. Roy Chowdhury, S. Dhara, I. Das, B. Bandyopadhyay, and R. Rawat, Large positive magnetoresistance in intermetallic compound $NdCo_2Si_2$, J. Magn. Magn. Mater. **451**, 625 (2018).

[5] L. Zeng, X. Hu, S. Guo, G. Lin, J. Song, K. Li, Y. He, Y. Huang, C. Zhang, P. Yu, J. Ma, D.-X. Yao, and H. Luo, Ta_4CoSi: A tantalum-rich superconductor with a honeycomb network structure, Phys. Rev. B **106**, 134501 (2022).

[6] G. Ryu, S. W. Kim, S. Matsuishi, H. Kawaji, and H. Hosono, Superconductivity in Nb_4MSi (M = Ni, Co, and Fe) with a quasi-two-dimensional Nb network, Phys. Rev. B **84**, 224518 (2011).

[7] J. Nagamatsu, N. Nakagawa, T. Muranaka, Y. Zenitani, and J. Akimitsu, Superconductivity at 39 K in magnesium diboride, Nature (London) **410**, 63 (2001).

[8] G. Profeta, M. Calandra, and F. Mauri, Phonon-mediated superconductivity in graphene by lithium deposition, Nat. Phys. **8**, 131 (2012).

[9] B. M. Ludbrook, G. Levy, P. Nigge, M. Zonno, M. Schneider, D. J. Dvorak, C. N. Veenstra, S. Zhdanovich, D. Wong, P. Dosanjh, C. Straßer, A. Stöhr, S. Forti, C. R. Ast, U. Starke, and A. Damascelli, Evidence for superconductivity in Li-decorated monolayer graphene, Proc. Natl. Acad. Sci. USA **112**, 11795 (2015).

[10] J. Chapman, Y. Su, C. A. Howard, D. Kundys, A. N. Grigorenko, F. Guinea, A. K. Geim, I. V. Grigorieva, and R. R. Nair, Superconductivity in Ca-doped graphene laminates, Sci. Rep. **6**, 23254 (2016).

[11] M. Petrov, J. Bekaert, and M. V. Milošević, Superconductivity in gallenene, 2D Mater. **8**, 035056 (2021).

[12] C. Si, Z. Liu, W. Duan, and F. Liu, First-principles calculations on the effect of doping and biaxial tensile strain on electron-phonon coupling in graphene, Phys. Rev. Lett. **111**, 196802 (2013).

[13] J. Bekaert, A. Aperis, B. Partoens, P. M. Oppeneer, and M. V. Milošević, Evolution of multigap superconductivity in the atomically thin limit: Strain-enhanced three-gap superconductivity in monolayer MgB_2, Phys. Rev. B **96**, 094510 (2017).

[14] J. Bekaert, M. Petrov, A. Aperis, P. M. Oppeneer, and M. V. Milošević, Hydrogen-induced high-temperature superconductivity in two-dimensional materials: The example of hydrogenated monolayer MgB_2, Phys. Rev. Lett. **123**, 077001 (2019).

[15] X. Gonze, B. Amadon, G. Antonius, F. Arnardi, L. Baguet, J.-M. Beuken, J. Bieder, F. Bottin, J. Bouchet, E. Bousquet, N. Brouwer, F. Bruneval, G. Brunin, T. Cavignac, J.-B. Charraud, W. Chen, M. Côté, S. Cottenier, J. Denier, G. Geneste *et al.*, The ABINIT project: Impact, environment and recent developments, Comput. Phys. Commun. **248**, 107042 (2020).

[16] J. P. Perdew, K. Burke, and M. Ernzerhof, Generalized gradient approximation made simple, Phys. Rev. Lett. **77**, 3865 (1996).

[17] G. M. Eliashberg, Interactions between electrons and lattice vibrations in a superconductor, Sov. Phys. JETP **11**, 696 (1960).

[18] G. M. Eliashberg, Temperature Green's function for electrons in a superconductor, Sov. Phys. JETP **12**, 1000 (1961).

[19] F. Giustino, Electron-phonon interactions from first principles, Rev. Mod. Phys. **89**, 015003 (2017).

[20] W. L. McMillan, Transition temperature of strong-coupled superconductors, Phys. Rev. **167**, 331 (1968).

[21] P. B. Allen and R. C. Dynes, Transition temperature of strong-coupled superconductors reanalyzed, Phys. Rev. B **12**, 905 (1975).

[22] P. B. Allen and B. Mitrović, Theory of superconducting T_c, Solid State Phys. **37**, 1 (1983).

[23] P. Morel and P. W. Anderson, Calculation of the superconducting state parameters with retarded electron-phonon interaction, Phys. Rev. **125**, 1263 (1962).

[24] G. Grimvall, *The Electron-Phonon Interaction* (North Holland, Amsterdam, 1981).

[25] W. Setyawan and S. Curtarolo, High-throughput electronic band structure calculations: Challenges and tools, Comput. Mater. Sci. **49**, 299 (2010).

[26] T. G. Saunderson, J. F. Annett, B. Újfalussy, G. Csire, and M. Gradhand, Gap anisotropy in multiband superconductors based on multiple scattering theory, Phys. Rev. B **101**, 064510 (2020).

[27] L. N. Oliveira, E. K. U. Gross, and W. Kohn, Density-functional theory for superconductors, Phys. Rev. Lett. **60**, 2430 (1988).

[28] A. Aperis, P. Maldonado, and P. M. Oppeneer, *Ab initio* theory of magnetic-field-induced odd-frequency two-band superconductivity in MgB_2, Phys. Rev. B **92**, 054516 (2015).

[29] J. Bekaert, A. Aperis, B. Partoens, P. M. Oppeneer, and M. V. Milošević, Advanced first-principles theory of superconductivity including both lattice vibrations and spin fluctuations: The case of FeB_4, Phys. Rev. B **97**, 014503 (2018).

[30] S. Poncé, E. Margine, C. Verdi, and F. Giustino, EPW: Electron–phonon coupling, transport and superconducting properties using maximally localized Wannier functions, Comput. Phys. Commun. **209**, 116 (2016).